Surface of Room-Temperature-Stable Electride $[Ca_{24}Al_{28}O_{64}]^{4+}(e^-)_4$: Preparation and Its Characterization by Atomic-Resolution Scanning Tunneling Microscopy

Yoshitake Toda,[†] Yousuke Kubota,[‡] Masahiro Hirano,[†] Hiroyuki Hirayama,[‡] and Hideo Hosono[†,*]

[†]Frontier Research Center and Material and Structure Laboratory and [‡]Department of Materials Science and Engineering, Tokyo Institute of Technology, 4259 Nagatsuta, Midori-ku, Yokohama 226-8503, Japan

ABSTRACT The nanocage compound crystal $[Ca_{24}Al_{28}O_{64}]^{4+}(e^-)_4$ (C12A7:e^-) is a room-temperature-stable electride. Although bulk C12A7:e^- exhibits metallic conduction, the surface of an as-prepared sample or one prepared by mechanical fracture in ultrahigh vacuum is almost insulating and exhibits distinct non-ohmic contact. We studied whether the intrinsic surface of this electride exhibits metallic conduction or not by examining various conditions for preparing the intrinsic surface. A combination of sputtering with thermal annealing led to the emergence of metallic conductivity in a specific condition. Suitably prepared surfaces revealed ohmic contact even in an ambient atmosphere. Atomic-resolution scanning tunneling microscopy (STM) images of the surfaces were consistent with a structural model in which the cage structure in the bulk C12A7:e^- electride is conserved at the surface.

KEYWORDS: nanocage compound · nanoporous crystal · electride · surface structure analysis · surface modification · scanning probe microscope · calcium aluminate

Electrides are crystalline salts in which electrons act as anions.[1,2] Conventionally, electrides have been synthesized using alkali metal adducts of organic molecules[3,4] or inorganic molecular sieves.[5−8] However, they are chemically and thermally unstable[9] and decompose in inert atmospheres at temperatures above −40 °C or in an ambient atmosphere at lower temperatures by reactions with O_2 and/or H_2O.

However, the electride $[Ca_{24}Al_{28}O_{64}]^{4+}(e^-)_4$ (C12A7:e^-), which was stable in air up to approximately 400 °C,[10] was successfully synthesized recently.[11−14] The key to its stability is its unique crystal structure. C12A7:e^- consists of positively charged crystallographic cages with inner diameters of approximately 0.5 nm (Figure 1). Anionic electrons are weakly trapped in these cages. The rigid structure of the lattice framework with Ca−O and Al−O bonds prevents the anionic electrons in the cages from being attacked by O_2 and/or H_2O in the external environment.

The three-dimensionally connected cages and anionic electrons give a partially filled cage conduction band (CCB).[15−18] The presence of the CCB makes the C12A7:e^- electride metallic and gives it a low work function (approximately 2.4 eV).[19] Furthermore, the anionic electrons in the cages could be transferred easily to the adsorbate at the surface by quantum tunneling. Because of these properties, C12A7:e^- is a promising material for electron-emitting devices and as a chemical reductant. There have already been some reports of C12A7:e^- applied as an electron emitter,[20,21] an electron-injection layer in an organic LED,[22,23] a secondary electron emitter in a plasma display panel,[24] and a chemical reductant.[25]

However, C12A7:e^- surfaces are inevitably covered by an insulating contaminant layer.[19,20,26] In the synthesis of C12A7:e^- electride, $[Ca_{24}Al_{28}O_{64}]^{4+}(O^{2-})_2$ (C12A7:O^{2-})[27−29] mother crystals are heated in a Ti atmosphere to dope anionic electrons *via* extraction of O^{2-} in the cage.[30] Consequently, the C12A7:e^- surfaces are covered by thick Ti suboxide (TiO_x) layers. Even after mechanical and chemical peeling of the TiO_x layers, the surfaces were still insulated. The insulating surface layers degraded the device performance in the applications. Furthermore, they make it difficult to ascertain the intrinsic nature of the nanocage crystalline C12A7:e^- electride surfaces.

From fundamental and engineering viewpoints, it is highly desirable to develop a

* Address correspondence to hosono@msl.titech.ac.jp.

Received for review October 21, 2010 and accepted February 15, 2011.

Published online March 01, 2011
10.1021/nn102839k

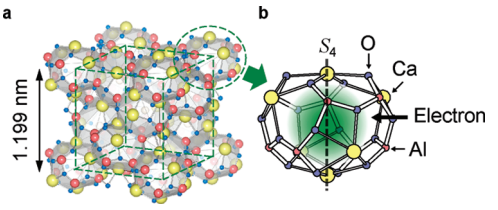

Figure 1. (a) Schematic illustration of the $[Ca_{24}Al_{28}O_{64}]^{4+}(e^-)_4$ (C12A7:e^-) crystal. The cube indicated by green dashed lines defines the cubic unit cell, which has a lattice constant of 1.199 nm and contains 12 cages. Yellow, red, and blue spheres represent Ca, Al, and O atoms, respectively, and white polygons represent the interior spaces of the cages and are approximately 0.5 nm in diameter. (b) Magnification of a cage with S_4 symmetry axes passing through two axial Ca ions and the cage center that can trap an electron (green-shaded region).

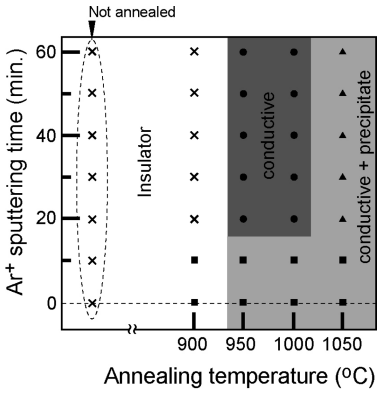

Figure 2. Surface treatment conditions and surface properties obtained through sputtering and annealing. Dark gray area: clean, metallic conductive, and relatively flat surfaces. Light gray area: surface was metallic conductive, but gray insulating phases appeared on the top surface. These insulating phases have different chemical components: closed triangles, Ca deficient; closed squares, not Ca deficient. White area: surface was insulating. Without sufficient sputtering (shorter than 20 min), gray insulating phases also appeared on the top surface (closed squares).

preparation method for clean and metallic conductive surfaces and to investigate the intrinsic surface properties of C12A7:e^- electride. However, to our knowledge, a cleaning method has not been established yet. The structure and stoichiometry of the C12A7:e^- surface are still unknown. Among the insulating materials in the $CaO-Al_2O_3$ system, the C12A7:e^- electride is exceptionally metallic conductive. Thus, a subtle discrepancy of the stoichiometry at the surface could result in the appearance of insulating surface phases such as $CaAl_2O_4$, $Ca_3Al_2O_7$, C12A7:O^{2-}, and amorphous C12A7:e^-. Even if the surface preserved the intrinsic stoichiometry, it is not certain whether the cage structure of the C12A7:e^- in the bulk would be preserved or not at the surfaces. Development of a cleaning method and atomically resolved scanning probe microscopy observation are necessary to address these fundamental questions for C12A7:e^- surfaces.

In this study, we examined Ar^+ ion sputtering and subsequent thermal annealing in ultrahigh vacuum (UHV) to obtain clean, metallic conductive, and relatively flat C12A7:e^- electride surfaces. Clean, stoichiometric, and metallic conductive surfaces were obtained only under certain conditions. Ohmic contact was obtained with the surfaces with metal electrodes even when the surfaces had been exposed to ambient conditions. Atomic-resolution scanning tunneling microscopy (STM) images of the surfaces could be interpreted consistently using a model in which the cage structure was conserved at the stoichiometric C12A7:e^- electride surfaces.

RESULTS AND DISCUSSION

Surface Preparation. As-prepared C12A7:e^- electride surfaces were insulating. We then tried to expose clean and metallic conductive surfaces by mechanical cleavage and sputter-annealing processes in a UHV apparatus equipped with an STM unit. The mechanically cleaved surfaces were rough on a millimeter scale due to the lack of a preferred cleavage plane in C12A7:e^- crystal. Furthermore, there was no tunneling current at sample bias voltages between −3 and +2 V, suggesting that the CCB at the Fermi level (the origin of the metallic conductivity of C12A7:e^- electride) does not exist at the cleaved surface, although a tunneling current was detected at +2.5 V. The lack of a CCB at the cleaved surface is also supported by a previous photoelectron emission study.[31] The study reported that the intrinsic CCB was observed at the Fermi level in bulk sensitive photoelectron spectroscopy with a photon energy of 8.4 eV but disappeared in surface sensitive photoelectron spectroscopy with a photon energy of 21.2 eV. From the lack of a preferred cleavage plane and intrinsic CCB (*i.e.*, metallic conductivity), we judged that mechanical cleavage was not a suitable surface preparation method. Instead, the sputter and annealing method was investigated thoroughly. We investigated which times and temperatures gave flat and metallic conductive clean surfaces.

Figure 2 summarizes the conditions required to obtain a metallic conductive surface in the sputter and annealing processes. Metallic conductive surfaces that the STM tip safely approached at any bias voltage between +3 and −3 V were obtained with a sputtering time of >20 min and subsequent annealing at 950 °C ≤ T ≤ 1000 °C (closed circles, Figure 2).

In contrast, gray insulating areas appeared in places on the surfaces when the annealing was performed at >1050 °C (closed triangles, Figure 2). *Ex situ* X-ray photoelectron spectroscopy (XPS) revealed that Ca was deficient in these areas. This suggests that high-temperature (>1050 °C) annealing causes preferential evaporation of Ca components. This in turn leads to the formation of a Ca-poor phase. In all the compounds in the $CaO-Al_2O_3$ system, only electron-doped C12A7 is particularly metallic conductive and electron-doping is

impossible for other phases. Thus, evaporation of Ca causes the formation of insulating areas during high-temperature annealing.

Gray insulating areas also appeared after annealing at $T \geq 900$ °C with sputtering times shorter than 20 min (closed squares, Figure 2). In contrast to the annealing at $T > 1050$ °C, *ex situ* XPS indicated that these gray areas were not deficient in Ca. When a sputtering yield of unity was assumed, approximately 1×10^{13} atoms cm^{-2} were estimated to be removed from the surface in the sputtering for 20 min. This surface atom density was equivalent to approximately 1/50 monolayer. Thus, sputtering removed only a small amount of the contaminating species adsorbed on the top of the sample surfaces. However, some of the contaminating adsorbates still remained at the top surface if the sputtering was insufficient. Substantially, O_2 and/or H_2O molecules in the ambient atmosphere are plausible candidates for these adsorbed species. An anionic electron in the cage of the C12A7:e^- electride is also easily replaced by O^{2-} during annealing under high pO_2.[10] Although no direct evidence has been reported, our recent studies on single-crystal growth of C12A7:e^- electride in an Ar atmosphere suggests that the anionic electron in the cage of the C12A7:e^- electride is easily exchanged with O^{2-} during annealing, even under very low pO_2 conditions. In growth under a conventional (oxygen-free) Ar atmosphere, the electron concentration in the cage stays to only 1×10^{20} cm^{-3},[32] while it reaches the theoretical maximum value of 2×10^{21} cm^{-3} under an Ar atmosphere with an O_2 getter ($pO_2 = 1 \times 10^{-22}$ Pa).[33] This difference in anionic electron concentration is reasonably attributed to the replacement of anionic electron by O^{2-}, which takes place even in extremely low pO_2 conditions. Therefore, a small amount of residual O_2 and/or H_2O surface species after insufficient sputtering could cause the formation of insulating small gray patches with O^{2-} and/or OH^- in the cages, even under UHV conditions. Therefore, annealing after insufficient sputtering produces insulating regions around these residual adsorbates. It is likely that this caused the appearance of the gray insulating areas in the samples annealed at $T \geq 900$ °C after insufficient sputtering.

With a sufficient sputtering time, annealing at $T > 950$ °C was necessary to produce a fully conductive surface. The lowest limit of the annealing temperature (950 °C) is close to the crystallization temperature of amorphous C12A7:e^- (950−1000 °C).[34] However, the dosage in the sputtering (1×10^{13} cm^{-2}) was sufficient to remove the small amount of surface contaminants but was too low to alter the crystalline framework of the surface to an amorphous state.[35] The surface cages are considered to have already been destroyed in the initial peeling process of the TiO_x layer because the surface lost its metallic conductivity, which is supported by the anionic electrons clathrated in the cages at this stage. We believe that annealing at 950−1000 °C is necessary to promote the recovery of the destroyed cages at the surface.

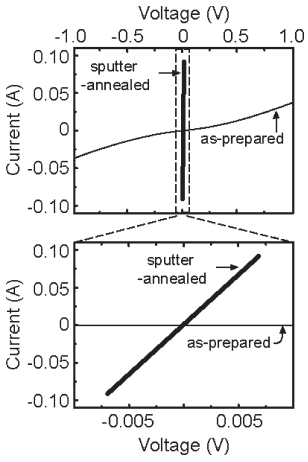

Figure 3. Current−voltage characteristics of the sputtered and annealed C12A7:e^- (thin line) and C12A7:e^- exposed to an ambient atmosphere (thick line). Voltage ranges are (top) ±1.0 V and (bottom) ±0.01 V.

Ohmic Contact. Figure 3 shows the *I*−*V* characteristics of the prepared sample (thin line) and a suitably sputtered and annealed sample (thick line). The measurement was carried out in an ambient atmosphere. The voltage range in the top panel is ±1 V and in the bottom panel is ±0.01 V. The top panel indicates that the current increased sharply with increasing voltage for the suitably sputtered and annealed sample, while a similar sharp rise was not observed in the other sample. The bottom panel confirms that the suitably sputtered and annealed sample had a linear (*i.e.*, ohmic) *I*−*V* dependence. The electrical conductivity was estimated to be 800 S cm^{-1} from the gradient. This is consistent with the value obtained by the four-probe method (approximately 1000 S cm^{-1}) in a separate experiment. This result demonstrates that the suitably sputtered and annealed surface preserved its metallic conductivity even after exposure to an ambient atmosphere. The robustness of the conductivity against exposure to an ambient atmosphere is consistent with the existence of surface cages. The cages stabilize anionic electrons by hindering the intrusion of small atmospheric molecules such as O_2 and/or H_2O.

STM Observation. Figure 4 shows typical large area (100×100 nm^2) (a) and magnified (10×10 nm^2) (b) STM images of the (100) surface. The surfaces were prepared by sputtering and annealing processes at 1000 °C for 1 h. The bias voltage applied to the samples was +2.5 V. The change in the bias voltage and polarity did not appear to influence the structures observed by STM. This indicates that the observed structure represents the topographical information of the surface. The surface was flat enough to enable STM analysis. Under STM (Figure 4a), the surface was covered in corrugations approximately 3 nm in size. No step and terrace

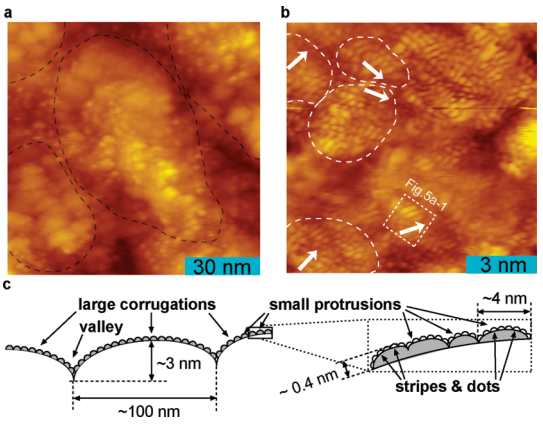

Figure 4. Typical STM images for a sputtered/annealed (100) surface over (a) a large area (100 × 100 nm^2) and (b) magnified area (10 × 10 nm^2), which were obtained using a sample bias voltage of +2.5 V. The large corrugations and small protrusions are enclosed by black and white dashed lines, respectively. White arrows indicate the alignment of the atomic dots. (c) Schematic side view of typical STM image for the sputtered/annealed surface.

structures were observed in the STM images. The flatness of the surface did not improve after annealing for a longer time (24 h) at temperatures above the crystallization temperature of amorphous C12A7:e$^-$.

In the large area STM image (Figure 4a), the large surface corrugations are the brighter areas enclosed in black dashed lines, and the darker areas are the valleys between these corrugations. These corrugations were 1−3 nm high. In addition, small protrusions 1−5 nm in lateral size and 0.2−0.4 nm in height were observed as bright areas distributed randomly on the large corrugations (Figure 4a). In the magnified STM image (Figure 4b), these small protrusions were observed as bright areas, and they are enclosed by white dashed lines in the figure. In Figure 4b, these small protrusions were measured to be 1−4 nm in diameter and 0.2−0.4 nm in height, which is consistent with the values measured in the large area STM (Figure 4a).

From the magnified STM images (Figure 4b), short lines of atomic-scale dots were observed on the small protrusions. These lines appeared to be aligned in particular directions on each small protrusion as indicated by the white arrows on Figure 4b. The direction of this alignment differed among the small protrusions. No long-range periodicity was observed at the surface. The (110) and (111) surfaces of the C12A7:e$^-$ samples sputtered and annealed under optimum conditions also showed the large corrugations, valleys, small protrusions, and atomic-scale dots similar to the (100) surfaces (Figure 4). The relationships among these structural features are schematically summarized in Figure 4c.

High-resolution (1.5 × 1.5 nm^2) STM images were used to study the atomic arrangement of the C12A7:e$^-$ samples sputtered and annealed under optimum conditions. Results for the (100), (110), and (111) surfaces

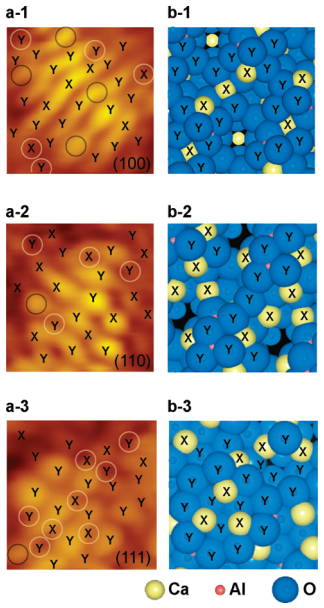

Figure 5. Comparison of obtained STM images with model surface structures. (a) High-resolution (1.5 × 1.5 nm^2) STM images for sputtered/annealed 1 (100), 2 (110), and 3 (111) surfaces taken with a sample bias voltage of +2.5 V. (b) Plan views of surface models for (100), (110), and (111) planes derived from the cage-conserved model. Yellow, red, and blue spheres denote Ca^{2+}, Al^{3+}, and O^{2-} ions, respectively. These models were drawn to the same scale as that of panel a. X and Y indicate the center points of Ca^{2+} and O^{2-} ions on the surfaces, respectively. Some inconsistencies were observed for areas indicated by black (excess atoms) and white (missing atoms) dotted curves in panel a.

are shown in Figure 5a. On the (100) surface (Figure 5a-1), atomic-scale dots were observed on the rows. The rows were parallel and were approximately 0.3 nm apart. On the rows, the dot-to-dot distance was also approximately 0.3 nm. Atomic-scale dots were also observed on the (110) and (111) surfaces with a dot-to-dot distance of approximately 0.3 nm.

Surface Structural Models. There are two possible intrinsic surface structures for the C12A7:e$^-$ electride; the broken-cage model and the cage-conserved model. Figure 6a shows the broken-cage model of the (100) surface, in which all of the surface cages are truncated by the (100) unit cell plane. The top view and cross-sectional view of the truncated surface are displayed in Figure 6a-1,a-2, respectively. The cage-conserved model of the (100) surface, in which all of the nanocages are conserved at the surface, is shown in Figure 6b. In both models, the cages are indicated by polygons in the cross-sectional view. The color of each polygon indicates the direction of the S_4 symmetry axis of the spheroidal cages in the C12A7:e$^-$ crystal (Figure 1b). According to the orientation of the S_4 symmetry axis, the cages are classified into six groups in the cross-sectional views as follows: $S_{4x}\pm$ (red), $S_{4y}\pm$ (green), and $S_{4z}\pm$ (blue) (Figure 6a-,b-1). In the top views (Figure 6 a-2,b-2), Ca^{2+}, Al^{3+}, and O^{2-} ions are indicated by yellow, red, and blue spheres, respectively. The position of the

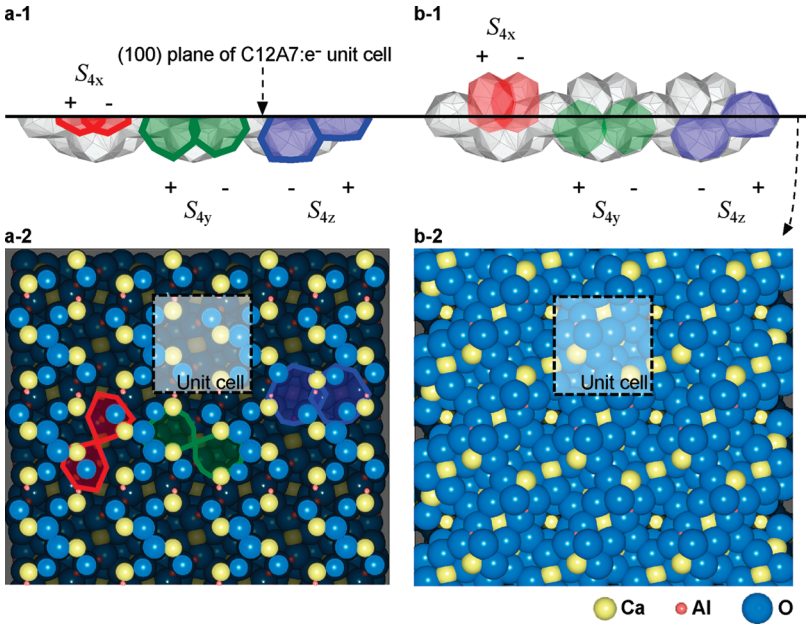

Figure 6. Cross-section and plan views of surface structural models for the (100) plane of C12A7:e$^-$. (a) Broken-cage model and (b) cage-conserved model. White polygons in the cross-sectional views represent the interior spaces of the cages. Yellow, red, and blue spheres in the plan views represent Ca^{2+}, Al^{3+}, and O^{2-} ions, respectively. Some Ca^{2+} ions located somewhat below the (100) cutting plane are indicated by the smaller yellow dots. The C12A7:e$^-$ crystal is composed of nanocages with spheroidal shapes. All cage structures have identical shapes but different orientations. The cages are classified into six groups based on the direction of their S_4 symmetry axis (shown in Figure 1b): $S_{4x}\pm$ (red), $S_{4y}\pm$ (green), and $S_{4z}\pm$ (blue). When a C12A7:e$^-$ (100) surface is cut (truncated) by a (100) unit cell plane, the semitransparent black regions in panel a-2 indicate open cages. Red, green, and blue polygons in the plan view of the broken-cage model indicate open mouths of destroyed cages. The colors correspond to those shown in the cross-sectional views.

ions with respect to the corrugations on the C12A7:e$^-$ crystal structure is represented by the brightness in each color, and brighter spheres indicate that the ions were at a higher position.

As shown in the top view of the models, the surface atom density of the top layer of the broken-cage model (Figure 6a-2) was lower than that of the cage-conserved model (Figure 6b-2). This is because the ions on the upper half of the cages at the top surface are missing in the broken-cage model. The low atom density generally causes an increase in the surface energy.[36] In addition, the broken cages cannot trap the anionic electrons, which causes the surface insulation. The properties of this model are inconsistent with the experimental results for surfaces sputtered and annealed under optimum conditions, which were thermally stable and electrically conductive. On the (110) and (111) surfaces, the broken-cage model is similar to that of the (100) surface, and it is inconsistent with the experimentally observed stability and metallic conductivity.

In contrast, the cage-conserved model enables the cages to trap anionic electrons at the top layer of the surface, and this causes the surface to be metallic conductive. Furthermore, the surface atoms have a large number of coordinated atoms and are expected to be energetically stable. Consequently, the cage-conserved model is more representative of the top surface layer structure of the sputtered and annealed C12A7:e$^-$ electride surfaces than the broken-cage model.

Comparison of STM Images with the Cage Conserved Surface Models. The STM images (Figure 5a) can be compared with the cage-conserved models at the (100), (110), and (111) surfaces (Figure 5b). The models are drawn to the same scale as the STM images (1.5×1.5 nm^2). Ca^{2+}, Al^{3+}, and O^{2-} ions are indicated by yellow, red, and blue spheres, respectively. The relative size of the spheres is proportional to the effective ionic radius of Ca^{2+} (0.10 nm), Al^{3+} (0.04 nm), and O^{2-} (0.14 nm).[37] In the cage-conserved models, Ca^{2+} and O^{2-} ions are dominant at the top surface layer, and the small Al^{3+} ions are tetrahedrally coordinated and obscured by the adjacent four O^{2-} ions. The Ca^{2+} and O^{2-} ions at the top surface layer are highlighted by the symbols X and Y, respectively, in the models of the (100), (110), and (111) surfaces (Figure 5b). The X and Y positions are transcribed in the STM images (Figure 5a) for comparison. The direction of the in-plane crystal axis could not be determined unambiguously in the experiment. Therefore, we rotated the structural models in-plane to maximize the consistency between the STM images and the structural models at each surface in Figure 5.

Almost all of the X and Y positions in the cage-conserved models coincided with the position of the bright dots in the STM images. This consistency arose because the cage-conserved model has a similar distance between the top surface layer ions (X and Y) to

that observed by STM (approximately 0.3 nm). The X and Y symbols also seem to align on the short lines in the cage-conserved models. The features in the STM images were reproduced well by the cage-conserved models at all of the surfaces.

However, on closer inspection, some of the protruding ions in the cage-conserved models were missing from the STM images as highlighted by the white-dashed circles in Figure 5a. Conversely, some protrusions in the STM images (indicated by the black-dashed circles in Figure 5a) had no corresponding ions in the cage-conserved models (Figure 5b). These minor discrepancies are probably because of structural relaxation of the nanocages at the surfaces. In the structural model, all cages were assumed to maintain their intrinsic spheroidal shapes at the surfaces. However, the surface cages lost their counterparts on the vacuum side. In the bulk, the atom keeps its position in the balance of the bonding forces from the neighboring atoms. However, at the surface, the atom lacks counterparts on the vacuum side and is therefore attracted toward the bulk direction under an imbalance of nearest neighbor interactions. This change results in surface tension generation. Cages at the surface are expected to feel the surface tension and be compressed slightly toward the bulk side. This compression induces relaxation of the cages, which is accompanied by the shift of some ions on the top half of the surface cages. Therefore, minor discrepancies between the STM images and the structural models could be tentatively attributed to the relaxation of the cages at the top surface layer. However, the effect of this relaxation cannot be estimated quantitatively.

The local structures with the aligned lines of atomic-scale dots in the STM images are fundamentally well explained by the cage-conserved structural model as described above. However, over a broader area the surface appeared to be corrugated (1−3 nm height) rather than flat. The corrugation amplitude was much larger than the radius of the surface cages (0.2−0.5 nm). This means that the surface cages were not truncated globally by a single plane but were truncated locally by planes of different heights. On these local truncation planes of different heights, the surface cages were restored. This probably explains why the surface did not show long-range ordered atomic arrangement. For example, the lines of atomic dots on the small protrusions were not all aligned in the same direction on the C12A7:e^- electride (100) surface (Figure 4b). This could be because of the difference in height of the corrugations in different areas of the surface. In the local model in Figure 5b-1, the surface is truncated by the (100) plane and then the truncated cages are restored as displayed in Figure 6b. Interestingly, the red ($S_{4x}\pm$) cages become the uppermost cages in this case. However, the bulk C12A7:e^- electride includes cages with six different rotational symmetries, including $S_{4x}\pm$, $S_{4y}\pm$, and $S_{4z}\pm$. Therefore, the corrugation results in the nonperiodic local appearance of all six types of cages at the top surface. Because the direction of the lines of atomic dots depends on the type of cage, the lines do not align in a unique direction, as observed in the STM image. However, local features such as the dot-to-dot distance and their alignment are still explained reasonably well by the cage-conserved model.

CONCLUSION

In this study, clean, relatively flat, and fully conductive C12A7:e^- electride surfaces were obtained by sputtering and annealing but only under limited conditions. The sputtering time had to be long enough (>20 min) to remove the contaminant from the surface, and the annealing temperature had to be between 950 and 1050 °C. Shorter sputtering times (<20 min) produced an insulating phase with OH^- or O^{2-} containing surface cages, while annealing at $T > 1050$ °C produced a Ca deficient insulating area. The annealing temperature needs to be high enough to recrystallize the mechanically damaged surfaces formed by the peeling of the TiO_x layers. The sputtered and annealed surfaces preserved ohmic contact even in an ambient atmosphere.

In atomic-resolution STM imagery, atomic scale dots that were spaced approximately 0.3 nm apart were observed to be aligned in short lines on the (100) and (110) surfaces. Most of the features in the STM images can be reasonably explained by the cage-conserved structural model. These results indicate that the nanocage structure was preserved but was somewhat relaxed vertically on the sputtered and annealed surfaces of the C12A7:e^- electride. The cage-conserved structure is also consistent with the stability and conductivity of the surfaces.

EXPERIMENTAL SECTION

C12A7:e^- single-crystal wafers were synthesized from an ingot of C12A7:O^{2-} mother crystal[38−40] grown by the Czochralski process.[39] The ingot was sliced into (100), (110), and (111) oriented wafers ($3 \times 10 \times 1$ mm^3). In these C12A7:O^{2-} wafers, O^{2-} ions were clathrated as free oxygen ions in the cages. The free oxygen ions were exchanged with anionic electrons by thermal annealing at 1100 °C for 24 h with Ti chips in an evacuated (10^{-1} Pa) silica glass tube.[30] The density of the anionic electron was estimated to be 2×10^{21} cm^{-3} from the optical absorption intensity at 2.8 eV. This indicated that all the free oxygen ions were completely replaced with anionic electrons in the wafers.

The C12A7:e^- wafers were covered by thin TiO_x layers as a result of the reaction of free oxygen ions with Ti. The TiO_x layers

were thoroughly removed by mechanical polishing with oil-based diamond powder slurries (9, 3, and 1 μm in diameter) or rinsing in very dry phosphoric acid at 290 °C for 1 min. The wafers were confirmed to be single-crystalline C12A7:e^- using X-ray diffraction.

After the TiO_x layer had been removed, the samples were transferred to an UHV system, which consisted of a load-lock chamber, a preparation chamber with a movable bar for cleavage and an Ar^+ ion gun, and a main chamber with an STM system (Unisoku, USM-1200S). The base pressures of the preparation and main chambers were lower than 1×10^{-8} Pa. We evaluated whether surfaces prepared by mechanical cleavage and by ion sputtering followed by annealing were metallic conductive. In mechanical cleavage procedure, the movable bar strikes the side of the sample to expose a cleaved surface. In the sputtering, Ar gas was introduced to the UHV chamber at 4×10^{-4} Pa. The sample surfaces were sputtered by Ar^+ ions (5 keV) at room temperature. The ion current was 4.8 nA/cm^2 at the sample surface. We used sputtering times of 0, 10, 20, 30, 40, 50, and 60 min. After sputtering, the chamber was evacuated to UHV again, and then annealing was performed *in situ* at room temperature, 900, 950, 1000, and 1050 °C for 1 h.

The flatness and atomic resolution of the structure of the metallic conductive surfaces were characterized *in situ* by STM. The STM tip was made from Pt−Ir alloy. The tip safely approached the metallic conductive surface at any bias voltage between +3 and −3 V, whereas the tip crashed when approaching the semiconducting or insulating surfaces, due to the absence of a tunneling current. On the basis of these tip approaching behaviors, we assessed whether the obtained surface was metallic or not. On metallic surfaces, STM images were obtained in constant current mode (0.05 nA). The cleanliness and stoichiometry of the surfaces was checked *ex situ* by X-ray photoelectron spectroscopy (XPS). Some of the metallic conductive samples were removed from the UHV system and submitted for resistivity measurements. Here, Pt foil electrodes (3×1 mm) were mechanically attached to these samples *ex situ*. The *I*−*V* characteristics were measured by the two-probe method in ambient conditions.

Acknowledgment. This study was supported by funds from the Element Science and Technology MEXT, Japan, and by the Funding Program for World-Leading Innovative R&D on Science and Technology, JSPS, Japan.

REFERENCES AND NOTES

1. Dye, J. L. Electrides—Ionic Salts with Electrons as the Anions. *Science* **1990,** *247*, 663–668.
2. Dye, J. L. Ionic Salts with Electrons as the Anions. *Science* **2003,** *301*, 607–608.
3. Dye, J. L. Electrides, Negatively Charged Metal-Ions, and Related Phenomena. *Prog. Inorg. Chem.* **1984,** *32*, 327–441.
4. Dye, J. L. Electrides: From 1D Heisenberg Chains to 2D Pseudo-Metals. *Inorg. Chem.* **1997,** *36*, 3816–3826.
5. Barrer, R. M.; Cole, J. F. Interaction of Sodium Vapour with Synthetic Sodalite−Sorption and Formation of Color Centers. *J. Phys. Chem. Solids* **1968,** *29*, 1755–1758.
6. Srdanov, V. I.; Stucky, G. D.; Lippma, E.; Engelhart, G. Evidence for an Antiferromagnetic Transition in a Zeolite-Supported Cubic Lattice of F Centers. *Phys. Rev. Lett.* **1998,** *80*, 2449–2452.
7. Petkov, V.; Billinge, S. J. L.; Vogt, T.; Ichimura, A. S.; Dye, J. L. Structure of Intercalated Cs in Zeolite ITQ-4: An Array of Metal Ions and Correlated Electrons Confined in a Pseudo-1D Nanoporous Host. *Phys. Rev. Lett.* **2002,** *89*, 075502.
8. Ichimura, A. S.; Dye, J. L.; Camblor, M. A.; Villaescusa, L. A. Toward Inorganic Electrides. *J. Am. Chem. Soc.* **2002,** *124*, 1170–1171.
9. Currently, the thermally stable organic electride has been synthesized. Redko, M. Y.; Jackson, J. E.; Huang, R. H.; Dye, J. L. Design and Synthesis of a Thermally Stable Organic Electride. *J. Am. Chem. Soc.* **2005,** *127*, 12416–12422.
10. Trofymluk, O.; Toda, Y.; Hosono, H.; Navrotsky, A. Energetics of Formation and Oxidation of Microporous Calcium Aluminates: A New Class of Electrides and Ionic Conductors. *Chem. Mater.* **2005,** *17*, 5574–5579.
11. Matsuishi, S.; Toda, Y.; Miyakawa, M.; Hayashi, K.; Kamiya, T.; Hirano, M.; Tanaka, I.; Hosono, H. High-Dnesity Electron Anion in a Nanoporous Single Crystal: $[Ca_{24}Al_{28}O_{64}]^{4+}$-$(4e^-)$. *Science* **2003,** *301*, 626–629.
12. Bertoni, M. I.; Mason, T. O.; Medvedeva, J. E.; Freeman, A. J.; Poppelmeier, K. R.; Delley, B. Tunable Conductivity and Conduction Mechanism in an Ultraviolet Light Activated Electronic Conductor. *J. Appl. Phys.* **2005,** *97*, 103713.
13. Palacios, L.; Torre, A. G. D. L.; Bruque, S.; Garcia-Munoz, J. L.; Garcia-Granda, S.; Sheptyakov, D.; Aranda, M. A. G. Crystal Structures and *In Situ* Formation Study of Mayenite Electrides. *Inorg. Chem.* **2007,** *46*, 4167–4176.
14. Lee, D. K.; Kogel, L.; Ebbinghaus, S. G.; Valov, I.; Wiemhoefer, H. D.; Lerch, M.; Janek, J. Defect Chemistry of the Cage Compound, $Ca_{12}Al_{14}O_{33-\delta}$—Understanding the Route from a Solid Electrolyte to a Semiconductor and Electride. *Phys. Chem. Chem. Phys.* **2009,** *11*, 3105–3114.
15. Sushko, P. V.; Shluger, A. L.; Hayashi, K.; Hirano, M.; Hosono, H. Electron Localization and a Confined Electron Gas in Nanoporous Inorganic Electrides. *Phys. Rev. Lett.* **2003,** *91*, 126401.
16. Li, Z.; Yang, J.; Hou, J. G.; Zhu, Q. Is Mayenite without Clathrated Oxygen an Inorganic Electride? *Angew Chem., Int. Ed.* **2004,** *43*, 6479–6482.
17. Sushko, P. V.; Shluger, A. L.; Hirano, M.; Hosono, H. From Insulatir to Electride: A Theoretical Model of Nanoporous Oxide $12CaO \cdot 7Al_2O_3$. *J. Am. Chem. Soc.* **2007,** *129*, 942–951.
18. Medvedeva, J. E.; Teasley, E. N.; Hoffman, M. D. Electronic Band Structure and Carrier Effective Mass in Calcium Aluminates. *Phys. Rev. B* **2007,** *76*, 155107.
19. Toda, Y.; Yanagi, H.; Ikenaga, E.; Kim, J. J.; Kobata, M.; Ueda, S.; Kamiya, T.; Hirano, M.; Kobayashi, K.; Hosono, H. Work Function of Room Temperature Stable Electride $[Ca_{24}Al_{28}O_{64}]^{4+}(e^-)_4$. *Adv. Mater.* **2007,** *19*, 3564–3569.
20. Toda, Y.; Matsuishi, S.; Hayashi, K.; Ueda, K.; Kamiya, T.; Hirano, M.; Hosono, H. Field Emission of Electron Anion Clathrated in Subnanometer-Sized Cages in $[Ca_{24}Al_{28}O_{64}]^{4+}(4e^-)$. *Adv. Mater.* **2004,** *16*, 685–689.
21. Toda, Y.; Kim, S. W.; Hayashi, K.; Hirano, M.; Hosono, H.; Haragichi, T.; Yasuda, H. Intense Thermal Field Electron Emission from Room-Temperature Stable Electride. *Appl. Phys. Lett.* **2005,** *87*, 254103.
22. Kim, K. B.; Kikuchi, M.; Miyakawa, M.; Yanagi, H.; Kamiya, T.; Hirano, M.; Hosono, H. Photoelectron Spectroscopic Study of C12A7:e^- and Alq3 Interface: The Formation of a Low Electron-Injection Barrier. *J. Phys. Chem. C* **2007,** *111*, 8403–8406.
23. Yanagi, H.; Kim, K. B.; Koizumi, I.; Kikuchi, M.; Hiramatsu, H.; Miyakawa, M.; Kamiya, T.; Hirano, M.; Hosono, H. Low Threshold Voltage and Carrier Injection Properties of Inverted Organic Light-Emitting Diodes with $[Ca_{24}Al_{28}O_{64}]^{4+}(4e^-)$ Cathode and $Cu_{2-x}Se$ Anode. *J. Phys. Chem. C* **2009,** *113*, 18379–18384.
24. Ono-Kuwahara, M.; Webster, S.; Ito, S.; Hosono, H. Highly Efficient Field Emission from a Spin-Coated Electride Powder. *SID Symposium Digest* **2006,** *37*, 1642.
25. Buchammagari, H.; Toda, Y.; Hirano, M.; Hosono, H.; Takeuchi, D.; Osakada, K. Room Temperature-Stable Electride as a Synthetic Organic Reagent: Application to Pinacol Coupling Reaction in Aqueous Media. *Org. Lett.* **2007,** *9*, 4287–4289.
26. Matsuishi, S.; Kim, S. W.; Kamiya, T.; Hirano, M.; Hosono, H. Localized and Delocalized Electrons in Room-Temperature Stable Electride $[Ca_{24}Al_{28}O_{64}]^{4+}(O^{2-})_{2-x}(e^-)_{2x}$: Analysis of Optical Reflectance Spectra. *J. Phys. Chem. C* **2008,** *112*, 4753–4760.
27. Bartl, H.; Scheller, H. T. Zur Struktur des $12CaO \cdot 7Al_2O_3$. *Neues Jahrb. Mineral. Monatsh.* **1970,** *35*, 547–552.
28. Chatterjee, A. K.; Zhmoidin, G. I. Phase Equilibrium Diagram of System CaO-Al_2O_3-CaF_2. *J. Mater. Sci.* **1972,** *7*, 93.

29. Taylor, H. F. W. *Cement Chemistry*, 2nd ed.; Thomas Telford: London, 1997.
30. Kim, S. W.; Matsuishi, S.; Nomura, T.; Kubota, Y.; Takata, M.; Hayashi, K.; Kamiya, T.; Hirano, M.; Hosono, H. Metallic State in a Line-Alumina Compound Realized by Relaxation of a Deformed Stoichiometric Crystal. *Nano Lett.* **2007,** *7*, 1138–1143.
31. Photoelectron spectroscopy study showing the lack of CCB at the mechanical cleaved surface has been reported. Souma, S.; Arakane, T.; Sato, T.; Takahashi, T.; Kim, S. W.; Matsuishi, S.; Hosono, H. Direct Evidence for Cage Conduction Band in Superconducting Cement $12CaO \cdot 7Al_2O_3$ by Low-Energy High-Resolution Photoemission Spectroscopy. *J. Phys. Soc. Jpn.* **2010,** *79*, 103704.
32. Yoon, S. G.; Kim, S. W.; Yoon, D. H.; Hirano, M.; Hosono, H. Single Crystal Growth of Nanoporous C12A7:e^- by Controlling Melt State. *J. Nanosci. Nanotechnol.* **2009,** *9*, 7345–7349.
33. Kim, S. W.; *et al.* unpublished.
34. Kim, S. W.; Miyakawa, M.; Hayashi, K.; Sakai, T.; Hirano, M.; Hosono, H. Simple and Efficient Fabrication of Room Temperature Stable Electride: Melt-Solidification and Glass Ceramics. *J. Am. Chem. Soc.* **2005,** *127*, 1370–1371.
35. Ar ion sputtering of 1×10^{13} cm^{-2} has been reported to cause point defects but not destroy the surface crystalline framework, for example, at Si(111) surfaces. Takashima, A.; Hirayama, H.; Takayanagi, K. Formation and Healing of Defects at the Si(111)7×7 Surface Under Low-Energy Ion Bombardment. *Phys. Rev. B* **1998,** *57*, 7292–7298.
36. Bechstedt, F. *Principles of Surface Physics*; Springer: Berlin, 2003.
37. Shannon, R. D. Revised Effective Ionic-Radii and Systematic Studies of Interatomic Distances in Halides and Chalcogenides. *Acta Crystallogr., Sect. A* **1976,** *32*, 751–767.
38. Watauchi, S.; Tanaka, I.; Hayashi, K.; Hirano, M.; Hosono, H. Crystal Growth of $Ca_{12}Al_{14}O_{33}$ by the Floating Zone Method. *J. Cryst. Growth* **2002,** *237*, 801–805.
39. Kurashige, K.; Toda, Y.; Matsuishi, S.; Hayashi, K.; Hirano, M.; Hosono, H. Czochralski Growth of $12CaO \cdot 7Al_2O_3$ Crystals. *Cryst. Growth Design* **2006,** *6*, 1602–1605.
40. Yoon, S. G.; Kim, S. W.; Hirano, M.; Yoon, D. H.; Hosono, H. Pore-Free $12CaO \cdot 7Al_2O_3$ Single-Crystal Growth by Melt State Control Using the Floating Zone Method. *Cryst. Growth Design* **2008,** *8*, 1271–1275.